

Interaction-driven giant electrostatic modulation of ion permeation in atomically small capillaries

Received: 6 May 2024

Accepted: 28 July 2025

Published online: 29 September 2025



Dhal Biswabhusan ¹, Yechan Noh ², Sanat Nalini Paltasingh ³, Chandrakar Naman ¹, Siva Sankar Nemala ⁴, Rathu Aparna ¹, Kaushik Suvigya ¹, Andrea Capasso ⁴, Saroj Kumar Nayak³, Li-Hsien Yeh ^{5,6} & Kalon Gopinadhan ^{1,7} ✉

Manipulating the electrostatic double layer and tuning the conductance in nanofluidic systems at salt concentrations of 100 mM or higher has been a persistent challenge. The primary reasons are (i) the short electrostatic proximity length, $\sim 3\text{--}10\text{ \AA}$, and (ii) difficulties in fabricating atomically small capillaries. Here, we successfully fabricate in-plane vermiculite laminates with transport heights of $\sim 3\text{--}5\text{ \AA}$, which exhibit a cation selectivity close to 1 even at a 1000 mM concentration, suggesting an overlapping electrostatic double layer. For gate voltages from -2 V to $+1\text{ V}$, the K^+ -intercalated vermiculite shows a remarkable conductivity modulation exceeding 1400% at a 1000 mM KCl concentration. The gated ON/OFF ratio is mostly unaffected by the ion concentration (10–1000 mM), which confirms that the electrostatic double layer overlaps with the collective ion movement within the channel with reduced activation energy. In contrast, vermiculite laminates intercalated with Ca^{2+} and Al^{3+} ions display reduced conductance with increasing negative gate voltage, highlighting the importance of ion-specific gating effects under \AA -scale confinement. Our findings contribute to a deeper understanding of electrostatic phenomena occurring in highly confined fluidic channels, opening the way to the exploration of the vast library of two-dimensional materials.

Selective and tunable ion transport is crucial in advanced material applications, including ‘lab-on-a-chip’ devices^{1,2}, energy harvesters^{3,4}, desalination membranes^{5,6} and neuromorphic devices^{7,8}. Among the many external stimuli affecting ionic transport, electrostatic gating appears to be highly reversible. Inspired by the remarkable efficiency of biological channels that rely on gated ion transport to activate certain functions⁹, researchers have explored the effects of electrostatic gating in several confined systems¹⁰. Although few experimental

groups have achieved reasonable gate modulation at dilute ion concentrations, little progress has been made at physiologically and practically relevant concentrations^{11–13} (i.e., 100 mM or higher). To be effective at high ion concentrations, the channels need to overcome electrostatic screening, which essentially restricts the channel size available for ion transport. The Debye length estimation at a 1000 mM KCl concentration suggests that the channel size should be smaller than 6 \AA . These challenging size requirements explain the

¹Department of Physics, Indian Institute of Technology Gandhinagar, Palaj, Gujarat 382355, India. ²Department of Physics, University of Colorado Boulder, Boulder, CO 80309, USA. ³School of Basic Sciences, Indian Institute of Technology Bhubaneswar, Khorda, Odisha 752050, India. ⁴International Iberian Nanotechnology Laboratory, Braga 4715-330, Portugal. ⁵Department of Chemical Engineering, National Taiwan University of Science and Technology, Taipei 10607, Taiwan. ⁶Advanced Manufacturing Research Center, National Taiwan University of Science and Technology, Taipei 10607, Taiwan. ⁷Department of Materials Engineering, Indian Institute of Technology Gandhinagar, Palaj, Gujarat 382355, India. ✉e-mail: gopinadhan.kalon@iitgn.ac.in

absence of works addressing high concentrations. Nevertheless, gating studies at dilute concentrations revealed several intriguing effects: dehydration of ions¹⁴, modification of interlayer interactions¹⁵, concentration polarization¹⁶, and ion sieving^{17,18}. In the past, several confined systems have been explored, such as silica nanochannels and nanowires¹¹, unintercalated graphene oxide (GO) laminates¹², MXenes¹³, MXene-GO [ref. 19,20] and TiO₂ nanochannels²¹. However, the majority of these systems have channel sizes > 7 Å. The best gate modulation effect reported thus far is < 1000% at concentrations as small as 10 mM.

At a high salt concentration (1000 mM), significant ion interaction effects are expected if the channel size is comparable to the Debye length, as demonstrated by molecular dynamics (MD) simulations^{22,23}. At this length scale, ion-ion and ion-water-ion interactions are likely to occur because of the close proximity of ions, water, and surfaces. Moreover, experiments can detect and study these effects. For example, the knock-on mechanism of ion transport due to Coulomb repulsion could lower the energy barrier and enhance the ionic conductance²⁴. Electrostatic gating of the fluidic surface can change the ionic concentration and their transport in highly confined channels. In addition to gating, the valency of the ions can also affect their interactions. In the very few studies, electrostatic gating was also found to alter ion-water interactions¹⁴.

Modulating ion transport at sea salt concentrations of 600 mM or higher is extremely difficult because of the requirement of highly confined fluidic channels, since the short Debye screening length at this concentration makes electrostatic gating ineffective. The focus of this paper is to modulate ion transport at these extreme concentrations, which is rarely discussed. There are many advantages of having high ion concentrations; for example, a high concentration ensures high ionic conductivity and hence a better signal-to-noise ratio. High concentrations may provide better stability against environmental fluctuations.

With this motivation, we designed channels with an overlapping electrostatic double layer (EDL) at high salt concentrations to assess the ion modulation and interaction effects. For this purpose, we fabricated laminates with angstrom-sized fluidic channels using earth-abundant and cost-effective vermiculite clay material. In vermiculites, the interlayer cations can be easily exchanged, thus providing a tunable transport height from ~3 to 5 Å. The atomically small interlayer space ensures that the Debye layer overlaps even at a 1000 mM concentration, enabling the selective and tunable transport of smaller cations such as K⁺ via electrostatic gating. The insulating membrane itself can serve as a gate dielectric, eliminating the need for an extra layer. The membrane is stable under aqueous conditions²⁵ and can operate at elevated temperatures²⁶.

Results and Discussion

Vermiculite crystals that occur naturally are composed of layers of magnesium aluminosilicate. Each layer is made up of three sheets: one octahedral sheet occupied by the Al³⁺ ion at the octahedral site can be substituted with Mg²⁺ or Fe²⁺, which is sandwiched between two tetrahedral sheets occupied by the Si⁴⁺ at the tetrahedral site (Fig. 1a) [ref. 27,28]. Additionally, Al³⁺ ions substituted one-fourth of the Si⁴⁺ ions in tetrahedral sites, causing an enhanced negative charge in the layered structure. These excess charges are balanced by cations such as Mg²⁺ or Ca²⁺ ions, which reside in the space between these layers. In our study, these Mg²⁺ cations were exchanged with other cations via the 2-step heat exchange approach described in the methods section. We intercalated K⁺, Ca²⁺, and Al³⁺ ions into vermiculite (V) laminates to achieve variable interlayer spacing. To estimate the interlayer spacing (*d*) of vermiculite laminates, we performed X-ray diffraction (XRD) on free-standing Li-V, K-V, Ca-V, and Al-V membranes in both dry and wet states (Supplementary Fig. 1a). We observe no significant difference in the peak positions of both states. Since we performed our ion transport measurements in a wet state, it is appropriate to discuss the

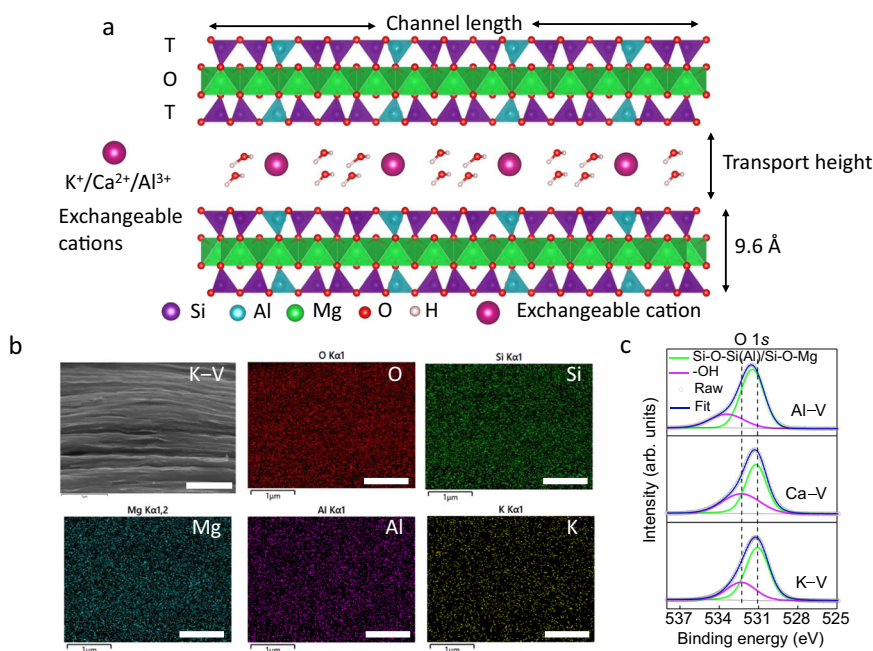


Fig. 1 | The structure of vermiculite and its composition. **a** Schematic of the vermiculite layers. The unit cell consists of tetrahedral and octahedral layers with Mg²⁺ occupying the octahedral sites and Si⁴⁺ and Al³⁺ the tetrahedral sites with shared oxygen. Exchangeable cations are occupied between the layers to balance the excess negative surface charge and are replaced with K⁺/Ca²⁺/Al³⁺ cations. **b** Energy dispersive spectroscopy (EDS) analysis of the elements across the layers of the K-V membrane indicates the presence of O, Si, Mg, Al, and the intercalant K. The scale bar

indicates 1 μm. **c** High-resolution X-ray photoelectron (XPS) spectra (XPS) of the K-V, Ca-V, and Al-V membranes. The grey open circle indicates the raw data of O 1s, and the blue line is the fitted data. Two deconvoluted spectra (green line and violet line) were derived from the raw data. The two black dotted straight lines indicate the peak position of -OH (violet) and Si-O-Si(Al)/Si-O-Mg (green) for K-V membranes. A clear shift of peak position towards higher binding energy is observed with increasing cation valence. Source data are provided as a Source Data file.

XRD results in the wet state. The XRD data revealed a '*d*' spacing of 12.2 Å for K–V. After subtracting the space occupied by the single magnesium aluminosilicate layer, which is 9.6 Å [ref. 29], we obtained a transport height of 2.6 Å for ion transport, which is occupied by solvated K^+ ions. Similarly, for the Ca–V and Al–V membranes, the transport height is 5.6 Å and 5.1 Å, respectively, occupied by hydrated Ca^{2+} and Al^{3+} ions. In the case of the Ca–V and Al–V membranes, higher-order peaks were observed, indicating complete laminated frameworks. Scanning electron microscope (SEM) cross-sectional images further confirmed the laminated structure (Supplementary Fig. 2) and helped us estimate the thickness of the membrane (i.e., $\sim 3.5 \mu\text{m}$). The cross-sectional energy dispersive spectroscopy (EDS) analysis of the K-intercalated vermiculite membrane revealed the main elements of vermiculite, such as O, Si, Mg, and Al, along with the intercalant K (Fig. 1b). The EDS maps of Ca–V and Al–V similarly show the intrinsic elements of vermiculite along with the intercalant (Supplementary Fig. 3a, b). However, intercalant Al is hard to distinguish from intrinsic Al. The membrane consists of monolayers with a thickness of 14 Å, as estimated from the AFM height profile (Supplementary Fig. 4). The mica-like structure adsorbs 1 or 2 layers of water molecules on its surface and hosts intercalated ions on its surface³⁰. This results in a slightly larger thickness of 14 Å instead of 9.6 Å.

Surface charges play a crucial role in controlling nanofluidic transport because the charged solid surface and electrolytes form an EDL [ref. 31], as proposed by Helmholtz in 1853. V-laminates feature a negative surface charge that draws cations to the interlayer space from the electrolytes, creating an EDL, which is confirmed by our zeta potential (Supplementary Fig. 5) and transport measurements. We employed several charged cation intercalants to control these zeta potentials. The zeta potential measurements of the K–V, Li–V, Ca–V, and Al–V solutions indicate that the K–V layers have a larger zeta potential of $-50 \pm 3 \text{ mV}$ than the Ca–V ($-19 \pm 3 \text{ mV}$) and Al–V ($-4 \pm 1 \text{ mV}$) layers. We also measured the zeta potential of the membranes; the values were very similar to those of the dispersed solution. The higher zeta potential value of the K–V solution indicates that more K^+ is needed to neutralize the surface than Ca^{2+} and Al^{3+} . This observation also suggests that in vermiculite, the surface charge can be easily controlled by the appropriate exchange of ions. The vermiculite membrane exhibited mechanical stability, with a tensile strength of $\sim 35 \text{ MPa}$ and a fracture strain of $\sim 2\%$ (Supplementary Fig. 6). This demonstrates that vermiculite is flexible and suitable for use in aqueous conditions.

Furthermore, we carried out a Fourier transform infrared (FTIR) spectroscopy study to confirm the presence of functional groups in the vermiculite. As described in Supplementary Fig. 7, the broad absorption peaks at 3360 cm^{-1} and 1643 cm^{-1} indicate the stretching and bending vibrations of the $-OH$ groups, respectively³². The absorbance peak at 970 cm^{-1} corresponds to the asymmetric stretching vibration of Si–O–Si. The two peaks at 735 cm^{-1} and 652 cm^{-1} are related to the Al–O–Al and M–O–Si (M is Mg, Al, and Fe) bonds, respectively^{29,32}. We also performed Raman analysis for all the cation-intercalated membranes, which revealed the characteristic peaks of Mg–O/Al–O and Si–O (Supplementary Fig. 8) [ref. 33].

We performed X-ray photoelectron spectroscopy (XPS) analysis on all the cation-intercalated membranes. The XPS survey of the K–V, Ca–V, and Al–V samples provided in Supplementary Fig. 9a shows common elements such as O, Si, Mg, and Al, along with intercalant atoms. The depth analysis of the intercalated cations indicates successful intercalation within the layers (Supplementary Fig. 9b–d). The O 1s deconvoluted spectrum has two peaks for K–V, one at 531.0 eV and the other at 532.3 eV, which corresponds to the Si–O–Si(Al)/Si–O–Mg and hydroxyl groups, respectively (Fig. 1c)^{34,35}. Both peaks shifted toward higher binding energy values with increasing cation valence, and the shift was maximal for Al-intercalated vermiculite, i.e., at 531.5 eV and 533.3 eV. The higher binding energy suggests that the electrostatic

interaction between Al^{3+} and the layers of vermiculite is considerable among all the intercalated vermiculite, which is in the order of $Al^{3+} - V > Ca^{2+} - V > K^+ - V$. A similar shift is also reported in the case of cation-intercalated montmorillonite membranes³³. A detailed analysis of the spectra corresponding to the elements of vermiculite, Si, Al, and Mg is provided in Supplementary Fig. 10.

Electrical modulation of ionic conductance measurements of angstrom capillary devices

We fabricated a voltage-gated device using various cation-exchanged vermiculite membranes. The membrane was initially cut into several pieces of size $5 \times 4 \text{ mm}^2$. These membrane pieces were further utilized to make the device. For the gate voltage, a gold wire was fixed onto a silver strip made in the middle of the membrane, which ensures a uniform gate voltage across the membrane (Fig. 2). This sample was then encapsulated between two acrylic blocks with the help of an epoxy (Loctite Stycast 1266), which isolated the gold gate electrode from the electrolytes. To expose both ends of the membrane, the sample was polished with P1000 emery sandpaper, and the final dimensions were confirmed via optical microscopy. The polished sample was sandwiched between two circular acrylic pieces with a prefabricated hole to ensure that ion transport occurred only through the vermiculite membrane (Fig. 2). The fabricated device had a length, *l* of 3 mm, and width, *w* of 4 mm. We performed all our measurements with these devices.

We performed ionic transport measurements in a homemade PEEK (polyether ether ketone) cell. The device was placed between two reservoirs containing aqueous salt solutions. Two homemade Ag/AgCl electrodes, labeled as the source and drain, were used for the ionic measurement. The ions were transported by applying a voltage, V_{ds} (drain to source voltage), and the resultant current, I_{ds} (drain to source current), was monitored. We used another source meter to apply a gate voltage (V_g) to the nanofluidic device, with the source as the ground terminal. A schematic of the measurement setup is shown in the inset of Fig. 3a. For the transport studies, we choose the right salt-exchanged membrane and solutions, for example, K–V membranes with KCl solutions, Ca–V membranes with $CaCl_2$ and Al–V membranes with $AlCl_3$, to avoid any ion exchange during the experiments. We prepared all the salt solutions with Milli-Q deionized water, and the final pH of the solution was 5–7; however, $AlCl_3$ is an exception, with a pH of 2.7 for a 1 mM chloride concentration. The pH values of the Li^+ , K^+ , Ca^{2+} , and Al^{3+} -intercalated vermiculite flakes dispersed in a 1 mM chloride solution were 7.2, 6.8, 7.1, and 5.6, respectively. It is clear from various characterizations that small changes in pH do not affect *d*-spacing or stability since equilibrium is achieved due to cation exchange. The sample temperature was maintained at 298 K for all the measurements, unless otherwise specified.

We first studied the effect of the gate voltage on the ion transport characteristics of a K–V sample. For this purpose, I_{ds} – V_{ds} characteristics were measured at different gate voltages, with V_g ranging from -2 V to $+1 \text{ V}$. The characteristics were mostly linear at low V_{ds} (Fig. 3a) for a 1000 mM KCl solution. There is a visible change in the slope of the curve with various V_g values. A finite zero-current voltage is observed for a larger negative V_g , plausibly indicating an asymmetric charge distribution. The larger positive current with negative V_g is attributed to the increased K^+ density and mobility, as supported by MD simulations presented later. The ionic conductance was extracted from the slope of the I_{ds} – V_{ds} plot. The KCl conductance across the membrane was reduced from $5.0 \mu\text{S}$ to $1.5 \mu\text{S}$ when V_g increased to $+1 \text{ V}$ (Fig. 3b). Conversely, the conductance value increased to $22.9 \mu\text{S}$ after applying a gate voltage of -2 V . The conductance increased by 1400% when V_g changed from $+1 \text{ V}$ to -2 V at a concentration of 1000 mM, which, to the best of our knowledge (comparison with other works is provided in Supplementary Table 1), is the highest ever reported (additional data can be found in Supplementary Fig. 11a, b). The conductance was

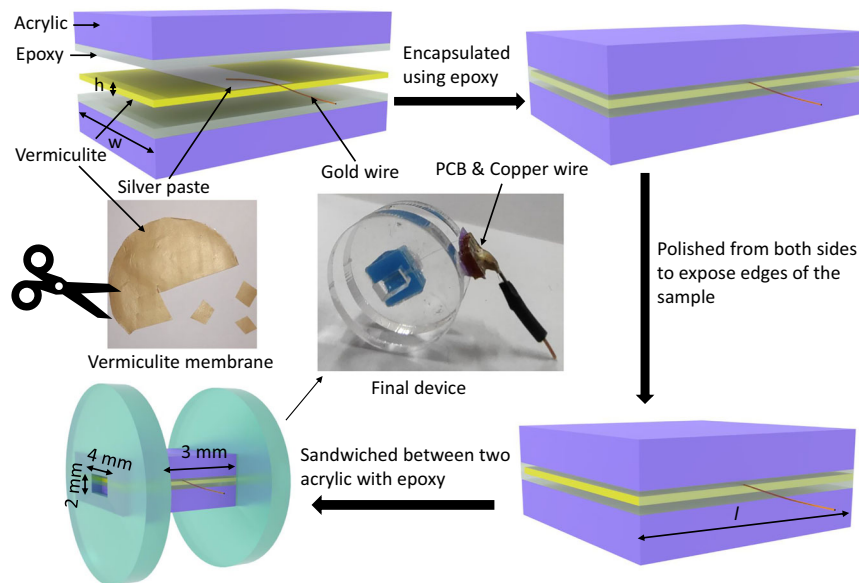


Fig. 2 | Fabrication of a voltage-gated sample. Schematics of various steps involved in the fabrication of voltage-gated vermiculite samples for studying gated ion transport characteristics. Here, h , w , and l are the thickness, width, and length

of the membrane, respectively. We used a gold wire to apply the gate voltage. The images are not drawn to scale.

highly reversible when V_g was tuned back to +1 V from −2 V (Supplementary Fig. 12a, b), a clear indicator of the stability of our devices. Furthermore, at the end of each gate voltage cycle, we measured the water conductance to check the integrity of our devices. More than 90% of our devices were found to be stable in this gate voltage range.

To understand the role of the EDL in ion transport, we examined the magnitude of voltage modulation at several KCl concentrations in the range of 1 mM–1000 mM. For this purpose, we defined a gating ON/OFF ratio, which is the ratio of conductance at $V_g = -2$ V to $V_g = +1$ V (Fig. 3c). The gating ON/OFF ratio is smaller at a 1 mM concentration; however, it increases and saturates in the concentration range of 10 mM–1000 mM, which is very similar to the zero V_g conductance versus concentration behavior (Supplementary Fig. 13). The increase in the gating ON/OFF ratio with increasing concentration is unusual and strikingly different from the findings of other reports^{12,13}. It is therefore important to understand the reasons for the significant gate modulation effects at high KCl concentrations. For this, let us first consider the situation of zero gate voltage. The cations (K^+) from the KCl solution are drawn to the negatively charged vermiculite surface (Supplementary Note 1) and are screened by the K^+ ions when the channel surface is not subjected to any gate voltage. The electrolyte solution concentration and ion valence control the screening length, also known as the Debye length, λ_D , which can be computed via the following formula given as

$$\lambda_D = \sqrt{\frac{\epsilon RT}{\sum_{i=1}^N F^2 Z_i^2 C_{i,0}}} \quad (1)$$

where ϵ is the permittivity of the solution; R and T are the gas constant and temperature, respectively; F is the Faraday constant; N is the total number of ionic species; and Z_i and $C_{i,0}$ are the valence and bulk concentrations of the i^{th} ionic species, respectively. The above expression implies that the Debye length decreases with increasing ion concentration. For example, at a 1000 mM KCl concentration, λ_D is 3 Å. The transport height for the K–V laminate is 2.6 Å, which means that for KCl concentrations ranging from 1 mM to 1000 mM, the EDL overlaps. Because of this, the variation in ionic conductance with concentration is not significant (Supplementary Fig. 13). For example, the

conductance only slightly increased from 1.31 μ S to 5 μ S when the KCl concentration was varied from 1 mM to 1000 mM. This relatively small change in conductance, despite a three-orders-of-magnitude increase in concentrations, suggests that ion transport is dominated by surface effects rather than bulk diffusive transport, $G \propto C_0$ [ref. 36].

We tested whether the ion hydration shells are squeezed or the laminated membrane structure expanded upon an applied gate voltage (V_g). The in-situ XRD data (Supplementary Fig. 1b) confirm that the laminated structure remains intact after a high negative V_g is applied. We tried to quantify the softness of the ion hydration shell, i.e., the extent of ion–water interactions and their modification under the influence of a gate voltage. We performed ionic conductance measurements at several temperatures and gate voltages to extract the activation energy (E_a). Figure 3d displays the Arrhenius plot between $\ln(G)$ and $1/T$, at different V_g values. E_a is calculated using the following formula

$$G \propto \exp\left(\frac{-E_a}{RT}\right) \quad (2)$$

where R is the universal gas constant, and the sample temperature T , varies from 25 to 60 °C. Our diffusion study revealed that K–V laminates are cation-selective due to the high density of negative surface charges (Supplementary Fig. 14a, b & Supplementary Table 2). Therefore, we can readily ascribe the activation energy, E_a , to that of K^+ ions. At 0 V_g , E_a is 298 meV. When V_g is +1 V, the E_a value increases to 309 meV, which explains the reduced ionic conductance observed for positive V_g (Fig. 3b). Interestingly, when $V_g = -2$ V, E_a decreased from 298 meV to 287 meV. The existence of a threshold voltage ($V_g \approx -1$ V) and the lower E_a (hence increased conductance) for $V_g < -1$ V suggests a modification in ion–water (hydration) interactions around K^+ ions.

We examined the impact of the gate voltage on the transport of higher valency cations using the electrolytes $CaCl_2$ and $AlCl_3$, and the conductance vs. concentration characteristics at 0 V_g are displayed in Supplementary Fig. 15a, b. Figure 4a shows the I – V characteristics at different V_g values for 500 mM $CaCl_2$ solutions. There is a visible change in the slope of the I – V curves with V_g . However, the current at zero voltage is lower than that of KCl solutions, especially for negative V_g . Figure 4b shows the influence of the gate potential on the ionic

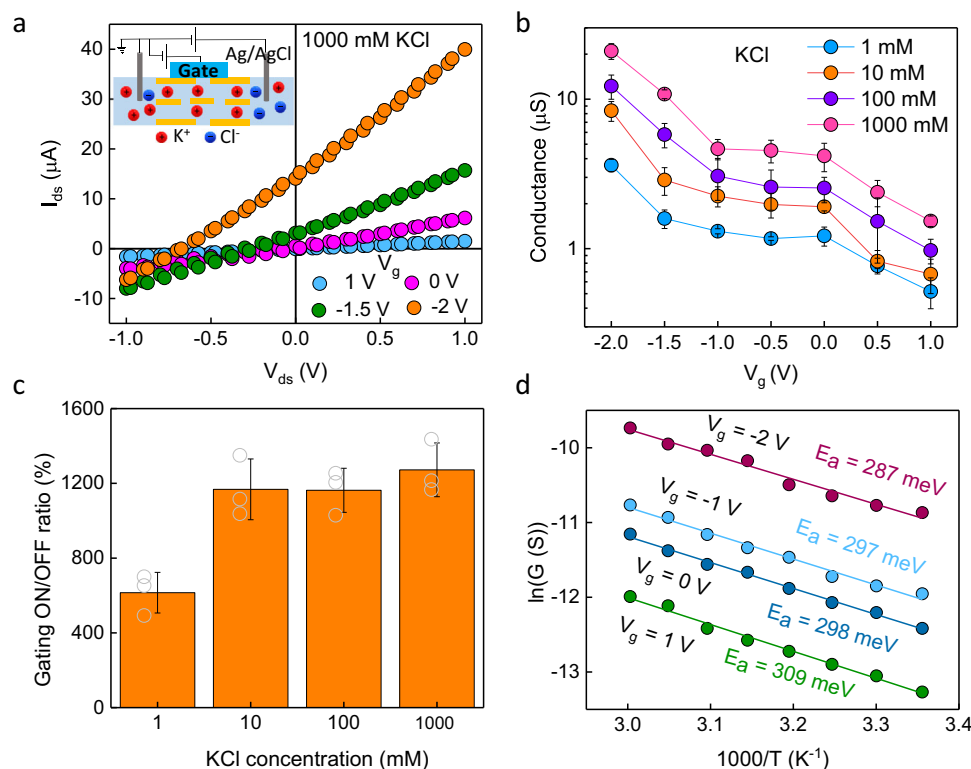


Fig. 3 | Electric field modulated ion transport through the K-V membrane.

a Modulation of the ionic current, I_{ds} with different V_g values from -2 V to $+1$ V in steps of 0.5 V in 1000 mM KCl solution. Inset: schematic of the voltage-gated device used for the transport measurement. **b** Variation in conductance with gate potential for 1 mM, 10 mM, 100 mM, and 1000 mM KCl. Data are presented as mean values \pm standard deviation. $N = 3$ independent samples. **c** Gating ON/OFF ratio (%)

between conductance at -2 V to $+1$ V for the several concentrations of KCl from 1 to 1000 mM. Data are presented as mean values \pm standard deviation. $N = 3$ independent samples. **d** Arrhenius plot for 1000 mM KCl showing the activation energy at several V_g values, the solid lines represent a linear fit. Source data are provided as a Source Data file.

conductance of CaCl_2 solutions at a concentration of 500 mM. For positive V_g , we observe a reduction in the CaCl_2 conductance upon an increase in V_g , similar to that of KCl solutions. However, for negative V_g , the conductance reaches a maximum at $V_g \approx -1$ V, beyond which it decreases. We performed these measurements at several chloride concentrations ranging from 1 mM to 1000 mM (Fig. 4b). When we increased the solution concentration from 1 mM, the maximum conductance, which occurred at around $V_g \approx -1$ V for all the concentrations, also increased. We also wanted to confirm whether this observation holds for a trivalent cation such as Al^{3+} . For this purpose, we chose aqueous solutions of AlCl_3 with chloride concentrations ranging from 1 mM to 1000 mM. In this case, we also observed a maximum in the conductance, but at $V_g \approx 0$ V (Fig. 4c, d). The maximum conductance increased when we increased the solution concentration, a trend similar to that of CaCl_2 solutions.

The zero V_g conductance of CaCl_2 and AlCl_3 is lower than that of KCl. Our estimated transport height for Ca-V and Al-V is 5.6 Å and 5.1 Å, respectively. It can accommodate 1 – 2 layers of water molecules as the bare sizes of Ca^{2+} and Al^{3+} ions are 2.02 Å and 1.06 Å, respectively³⁷. Theoretical studies suggest that the first hydration layer is very strong in the case of Ca^{2+} and Al^{3+} , which is difficult to remove as penalties of -1504 kJ/mol and -4665 kJ/mol energy are needed, respectively³⁷. Therefore, major modification in the ion–water interaction is unlikely even with the largest V_g that we have applied. Like in KCl solutions, the CaCl_2 and AlCl_3 conductance saturates at high concentrations (Supplementary Fig. 15a, b). Contrary to the KCl results, we observed a decrease in conductance with negative V_g , which suggests the emergence of a different interaction. Moreover, the maximum conductance decreases with decreasing ion concentration. Our diffusion data (Supplementary Fig. 14a, b) and zeta potential

measurements (Supplementary Fig. 5) indicate that the cation selectivity of vermiculite is in the order of $\text{KCl} > \text{CaCl}_2 > \text{AlCl}_3$.

We observed that the gate voltage dependent ionic conductance behavior of vermiculite laminates that are intercalated with KCl, CaCl_2 , and AlCl_3 solutions is strikingly different from other reported membranes that are unintercalated, such as on MXenes¹³. The possibility of water splitting at extreme values of V_g is ruled out simply because the conductance of CaCl_2 and AlCl_3 solutions decreases with V_g beyond -1 V. In the case of K^+ ion transport through K-V laminates, we see a nonmonotonic increase in conductance with negative V_g . Recently, an atomic transistor consisting of rGO showed an increase in K^+ transport when a gate voltage was applied¹⁴. In this case, the density of ions increases, and the barrier energy for ions decreases with V_g , which results in increased conductance. The barrier energy is exponentially related to the ion mobility (μ) as

$$\mu = \mu_0 \exp\left(\frac{-E_a}{kT}\right) \quad (3)$$

where μ_0 is the bulk ion mobility (i.e. for K^+ , $\mu_0 = 7.62 \times 10^{-8} \text{ m}^2 \text{ V}^{-1} \text{ s}^{-1}$). A decrease in the barrier energy clearly leads to an increase in ion mobility and hence in the conductance.

We also checked whether the gating ON/OFF ratio depends on the cation's energy barrier. For this purpose, we chose a Na-V membrane with NaCl solutions at a concentration of 1000 mM. We found that the gating ON/OFF ratio decreased to $\sim 1100\%$ (Supplementary Fig. 16a, b), which could be due to its (Na^+) slightly larger hydration barrier than K^+ . Additionally, with increasing membrane thickness (K-V, $h = 8 \mu\text{m}$), the overall ionic conductance increases, but the gating ON/OFF ratio decreases to $\sim 1100\%$ (Supplementary Fig. 17a, b). This result suggests

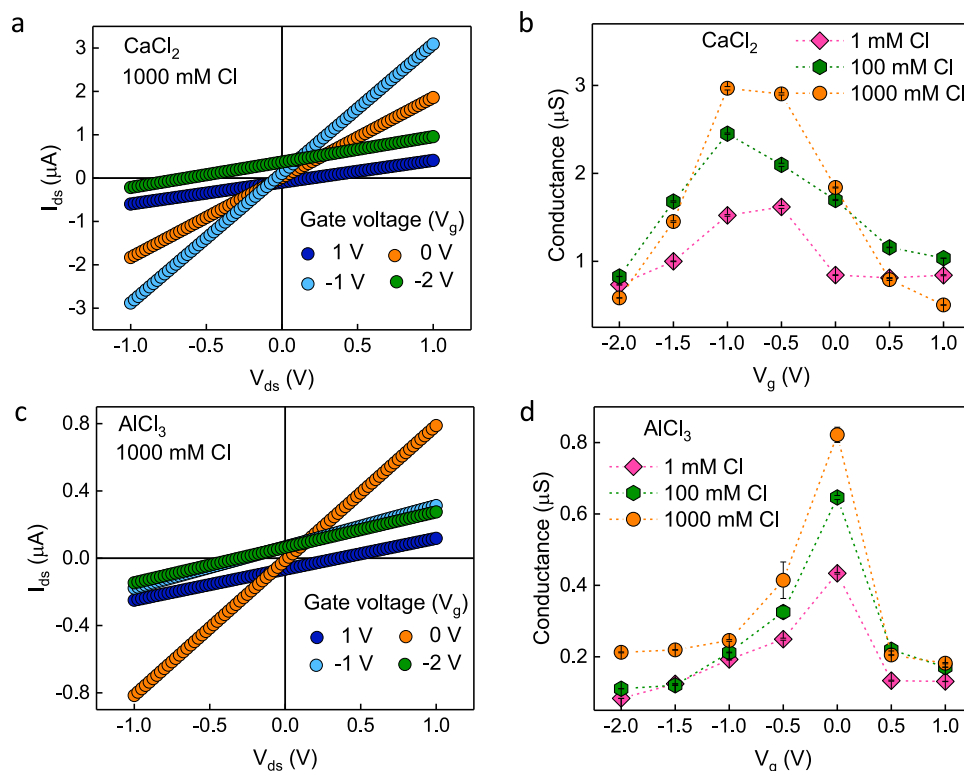


Fig. 4 | Voltage-gated ion transport through Ca-V and Al-V devices, and the effect of ion valence. **a** Variation in the ionic current, I_{ds} with the applied potential, V_{ds} , for 500 mM CaCl_2 solutions at various V_g . **b** Conductance vs V_g plot for 0.5 mM, 50 mM, and 500 mM CaCl_2 solutions. Data are presented as mean values \pm standard deviation. $N = 3$ independent measurements. **c** Variation in the ionic current, I_{ds}

with the applied potential, V_{ds} , for 333 mM AlCl_3 solutions at various V_g . **d** Conductance vs V_g plot for 0.33 mM, 33 mM, and 333 mM AlCl_3 solutions. Data are presented as mean values \pm standard deviation. $N = 3$ independent measurements. Source data are provided as a Source Data file.

that the gating effect might be more pronounced in thinner than in thicker membranes.

To understand the ion transport mechanism under gate voltages for K-V and Ca-V systems, we conducted all-atom MD simulations. The MD simulation setup is illustrated in Fig. 5a. We considered transport heights of 2.6 Å and 5.6 Å for the 1000 mM KCl and 500 mM CaCl_2 systems, respectively, matching the experimental values. To emulate the gating effect, a net charge ΔQ_{net} was introduced to the membrane atoms³⁸ using the distribution equation as

$$\Delta q_i = \Delta Q_{\text{net}} \frac{|q_i|}{\sum_i |q_i|} \quad (4)$$

where q_i represents the partial charge of atom i in the membrane. The charge modification applied was within 1.5% of the original partial charge. Ideally, the surface charge density, σ , has a linear relation with V_g which is given below

$$\sigma = \frac{\Delta Q_{\text{net}} + Q_0}{A} = CV_g + \sigma_0 \quad (5)$$

where A is the surface area, C is the capacitance, and Q_0 and σ_0 are the net charge of the membrane and the surface charge density at $V_g = 0$, respectively. An external electric field corresponding to 1 V was applied to induce ion transport. Additional methodological details of the MD simulations are provided in the Methods section.

The surface of the vermiculite membrane is terminated with oxygen atoms, naturally generating negative electrostatic dipoles directed toward the interlayer space, thereby providing binding sites for cations. This locally negative electrostatic environment within the highly confined vermiculite interlayer attracts cations, even when the

membrane is electrically neutral. Figure 5b shows snapshots of ions in K-V and Ca-V systems, demonstrating that a negative gate voltage generally increases the population of intercalated cations, whereas a positive gate voltage decreases it. Note that cation transport through this highly confined space involves a sequential hopping process between binding sites created by the oxygen-terminated surface. Such a sequential, barrier-leaping ion transport mechanism has been historically studied in the context of biological nanochannels³⁹ and has also been documented in synthetic membranes⁴⁰. Our MD simulations for cation currents in the K-V and Ca-V systems show qualitatively consistent trends with the experimental observations (Fig. 5c, d). In the K-V system, the cation current increases with decreasing σ (decreasing V_g), whereas the Ca-V system exhibits a peak current at a specific σ value. We calculated average ion density within the interlayer space as a function of surface charge density (see Fig. 5e, f). In the K-V system (2.6 Å), only K^+ ions intercalate, whereas in Ca-V systems (5.6 Å), both Ca^{2+} and Cl^- ions occupy the interlayer space. Figure 5g, h shows the average mobility of ions between the membranes. In the K-V system, K^+ mobility increases with decreasing surface charge. In the Ca-V system, the Ca^{2+} mobility peaks at $\sigma \approx -0.4 \text{ C/m}^2$, whereas the Cl^- mobility decreases with decreasing σ .

We closely examined ion trajectories at different gate voltages in our MD simulation, leading to the following insights into ion transport mechanisms (illustrated in Fig. 5b): For the K-V system at negative V_g , the density of K^+ increases and K^+ ions undergo frequent, short-distance hopping, resulting in high current (Supplementary Movie 1). At a positive V_g , K^+ ions become depleted and exhibit infrequent hopping over relatively long distances, leading to a low current (Supplementary Movie 2). For the Ca-V system, Ca^{2+} ions become less mobile at strongly negative V_g because of the strong Ca-V interaction (Supplementary Movie 3). At positive V_g , Ca^{2+} and Cl^- ions move in

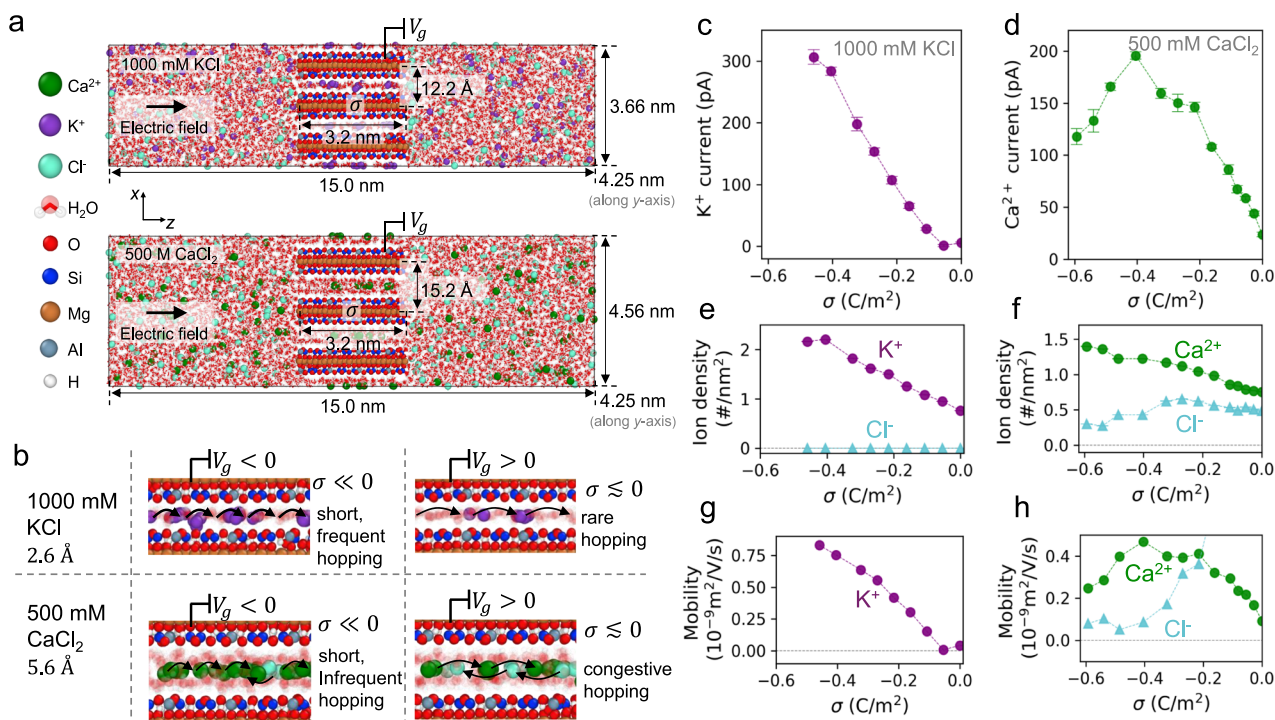


Fig. 5 | Molecular dynamics (MD) simulation of ion transport through Å-scale 2D vermiculite membranes. **a** Snapshot of the simulation systems for 1000 mM KCl (top) and 500 mM CaCl₂ (bottom) solutions. **b** Effect of the gating voltage on the ion distribution and transport through the vermiculite interlayer spacing. **c–d** Cation current as a function of surface charge density for **c** 1000 mM KCl and **d** 500 mM CaCl₂. The error bars for the current were estimated as the standard deviation of the slope obtained from a linear regression of the flux-time data, sampled every 50 ps over a total simulation time of 200 ns. The centre of the error

bar is the mean. **e, f** Density of intercalated ion as a function of surface charge density for **e** 1000 mM KCl and **f** 500 mM CaCl₂. The error bars for the ion density were estimated as the standard deviation of the ion density, sampled every 50 ps over a total simulation time of 200 ns. The centre of the error bar is the mean. **g, h** Mobility of intercalated ions as a function of surface charge density for **g** 1000 mM KCl and **h** 500 mM CaCl₂. Source data are provided as a Source Data file.

opposite directions, interfering with each other's transport and resulting in a congested hopping process that reduces Ca²⁺ mobility (Supplementary Movie 4). As a result of reduced mobility at both the negative and positive V_g limits, the Ca²⁺ current reaches its maximum at the intermediate V_g value (Supplementary Movie 5). Theoretically, the mobility of K⁺ ions can also be reduced at even higher negative surface charges. To further understand the effect of gating on ionic mobility within these Å scale channels, an energetic analysis of each ion may be necessary, although this is beyond the scope of this work.

We also investigated a commonly used GO system to infer the gating effect at 1000 mM, where the Debye length does not overlap with the transport height (~ 7 Å). We found no evidence of a gating effect (Fig. S18a–d).

The significant electric field effect observed in vermiculite membranes is a result of (i) the considerable length of the gate electrodes (~ 2 mm), which enhances cation accumulation when negative gate voltages are applied, and (ii) the ~ 1 nm thick insulating vermiculite layers capacitively induce charges, and the presence of 1 to 2 layers of water ensures weaker electrostatic screening, resulting in a field effect on the fluidic channels. Theoretical simulations indicate that thinner dielectric layers induce higher surface charge and zeta potential⁴¹. Recent reports of the electric field effect in conducting membranes such as GO and MXenes without the use of a gate oxide for gating are puzzling; however, it may be argued that there are thin insulating layers in the form of functional groups, which might help induce surface charges and hence tunability of conductance or permeation. Our device configuration is inspired by solid-state field-effect transistors; thus, the interpretation of the results is straightforward. Mica has a very high breakdown strength of 12 MV/cm [ref. 42], which is expected to be similar for vermiculite. Therefore, the probability of the

formation of conducting filaments in our membranes is very unlikely since our maximum applied voltage is only 2 V across a membrane thickness of 3.5 μ m.

The gated ion transport device demonstrated in our study is effective in modulating the conductance of monovalent ions and, as such, holds promise for several advanced applications. First, the precise control over ion flow in angstrom-scale channels makes these devices excellent candidates for lab-on-chip systems, where accurate dosing and real-time regulation of ionic species are critical. For instance, in controlled drug delivery, the ability to selectively modulate the transport of monovalent ions could be leveraged to trigger downstream chemical or biological processes with high temporal resolution. Additionally, the distinct response observed for monovalent *vs.* multivalent ions—evidenced by the contrasting transconductance behavior under negative gate voltages—suggests that these devices could be engineered to separate ions based on their valence. This selective ion separation could have significant implications in water purification, where the removal of specific ion types is desired, as well as in the design of fuel cells and batteries. In these energy applications, energy-efficient ion gating is essential to optimize performance and reduce losses. The inherent modularity of the vermiculite membrane system allows for further functionalization. For example, by incorporating inorganic pillars (such as alumina) to expand the van der Waals gap, the device architecture could be tuned to accommodate larger species⁴³. This would enable the transport of biomolecules (e.g., DNA, RNA, proteins), finding applications in biosensing and gate-controlled sequencing and detection platforms.

We demonstrated how gate voltage alters ion-water and ion-surface interactions at room temperature in highly confined vermiculite laminates. Negative gate voltages increased the cation

concentration inside the channels, resulting in unusual ion gating effects. We observed a sizeable ionic conductance modulation of $\sim 1400\%$ in 1000 mM KCl solutions. In the same voltage range, much-reduced conductance modulation was observed in the CaCl_2 and AlCl_3 solutions, resulting from ion-surface interactions inferred from the MD simulations. Future research must focus on high salt concentrations and extreme confinements to understand and explore the whole dynamics of ion interaction effects. This study reveals how to treat industrial waste of high salt concentrations efficiently. Overall, two-dimensional materials offer endless possibilities for fabricating tunable channels at the Å-scale.

Methods

Chemicals

Natural vermiculite crystals (2–3 mm in size), potassium chloride (KCl, $\geq 98.5\%$), sodium chloride (NaCl, $\geq 99.0\%$), lithium chloride (LiCl, $\geq 99.0\%$), calcium chloride (CaCl_2 , $\geq 98.0\%$), aluminum chloride (AlCl_3 , $\geq 97.0\%$), PVDF (0.22 μm pore size), and silver paste were purchased from Sigma Aldrich. All the chemicals purchased were used as received. Gold wire (30 μm in diameter) was purchased from Tanaka K.K. (Japan).

Fabrication of vermiculite laminates

The natural vermiculite crystals obtained were thermally expanded, and the cations were exchanged via a two-step method²⁵. Briefly, in the first step, 100 mg of vermiculite crystals were soaked in a 200 mL saturated NaCl solution and refluxed for 24 h at 100 °C, followed by washing with deionized water 8 to 10 times to remove excess salts. During this process, interlayer Mg^{2+} cations are exchanged with Na^+ ions. In the next step, the sodium-exchanged vermiculites were soaked in 200 mL of 2000 mM lithium chloride (LiCl) solution, refluxed for an additional 24 h, and again washed with DI water until excess chloride ions were removed. The resulting Li-exchanged vermiculite (Li-V) crystals were dried and dispersed in water at a 1 mg/mL concentration and sonicated for 30 min. The monolayers were obtained by centrifuging at $1509 \times g$ for 15 min or allowing the large flakes to settle in the solution overnight under gravity. We used the supernatant containing the monolayer to prepare the vermiculite membrane via vacuum filtration assembly. We used PVDF of 0.22 μm pore size as the support for vermiculite membranes, which easily peeled off after drying the samples under an IR lamp for 10 min. These free-standing membranes were dipped into 1000 mM chloride concentration of KCl, CaCl_2 , and AlCl_3 solutions for 24 h, which resulted in the intercalation of the cations K^+ , Ca^{2+} , and Al^{3+} , respectively, into the vermiculite interlayers. Our previous study²⁵ reported that the above cations make vermiculite membranes highly water-stable. We subsequently washed the cation exchanged membranes with water to remove excess salt from the surface and dried them under an IR lamp. These materials were further characterized and used for ion transport studies.

Characterization

A Rigaku Multipurpose X-ray diffractometer (XRD) with Cu K α radiation ($\lambda = 1.5406 \text{ \AA}$) was used to determine the interlayer spacing of the cation-exchanged vermiculite membranes. The thickness of the exfoliated vermiculite flake was determined using atomic force microscopy (Bruker Nano wizard Sense AFM), the membrane thickness was determined from cross-sectional SEM images (JEOL JSM-7900F), and a zeta potential measurement was carried out via DLS and Zeta Seizer instrument (Nano ZS Malvern Instrument). Energy dispersive spectroscopy analysis (EDS, JEOL JSM-7900F) was performed to determine the elements present in the vermiculite membranes. Fourier transform infrared spectroscopy (FTIR) (Perkin Elmer), and Raman spectroscopy (WITec) were used to confirm the functional groups present in vermiculite. For Raman spectroscopy, 532 nm laser light with 5 mW of

power was used for excitation at room temperature. X-ray photoelectron spectroscopy (XPS) was also carried out to determine the elemental details. XPS spectra were acquired with an ESCALAB 250 XI (Thermo Fisher Scientific, source: Mg K α 300 W, pass energy: 40 eV) system, where the analysis chamber was pumped down to ultrahigh vacuum (UHV $\sim 5 \times 10^{-10}$ mbar). The mechanical testing was carried out using a universal testing machine (UTM, model number- Kappa SS_CF100).

Molecular dynamics simulation

All-atom molecular dynamics (MD) simulations were performed to investigate ion transport through Å-scale two-dimensional (2D) vermiculite membranes. The simulations were conducted using periodic rectangular simulation boxes with dimensions of 3.66 nm \times 4.25 nm \times 15.0 nm (x, y, z) for the 1000 mM KCl system and 4.56 nm \times 4.25 nm \times 15.0 nm for the 500 mM CaCl_2 system. Three layers of vermiculite membranes were stacked along the x-direction and positioned at the center of the z-coordinate system, as depicted in Fig. 5a. The vermiculite membranes and ions were modelled using the Clay Force Field⁴⁴ and water molecules were described by the standard simple point charge (SPC) model⁴⁵. To emulate the gating effect of the membranes, a net charge (Q_{net}) was added to the membrane atoms using the distribution equation described in the main text. The systems were solvated with water molecules and ions with additional cations added to neutralize the system. The positions of the vermiculite membrane atoms were restrained using a harmonic spring. Prior to production runs, the system underwent an initial energy minimization, followed by equilibration under the NPT ensemble with a variable z-box size at 300 K and 1 bar for 2 ns. The barostat and thermostat relaxation times were set to 2 ps and 0.1 ps, respectively. Following equilibration, an external electric field of 0.067 V/nm was applied along the z-direction, corresponding to a 1 V transmembrane bias, and the simulation was conducted under the NVT ensemble. Ion transport simulations were performed for 200 ns, and the last 100 ns of trajectory data were used for analysis. All MD simulations were performed using a GPU-accelerated MD code with GROMACS^{46,47} version 2024.2, and atomic visualizations were generated using OVITO⁴⁸.

Reporting summary

Further information on research design is available in the Nature Portfolio Reporting Summary linked to this article.

Data availability

All data that are required to understand the conclusions in the paper are presented in the main manuscript and the Supplementary Information. Source data are provided with this paper.

References

- Di Trani, N. et al. Electrostatically gated nanofluidic membrane for ultra-low power controlled drug delivery. *Lab. Chip* **20**, 1562–1576 (2020).
- Kovarik, M. L. & Jacobson, S. C. Nanofluidics in lab-on-a-chip Devices. *Anal. Chem.* **81**, 7133–7140 (2009).
- Feng, J. et al. Single-layer MoS₂ nanopores as nanopower generators. *Nature* **536**, 197–200 (2016).
- van der Heyden, F. H. J., Bonthuis, D. J., Stein, D., Meyer, C. & Dekker, C. Electrokinetic energy conversion efficiency in nanofluidic channels. *Nano Lett.* **6**, 2232–2237 (2006).
- Homaeigohar, S. & Elbahri, M. Graphene membranes for water desalination. *NPG Asia Mater.* **9**, e427–e427 (2017).
- Oviroh, P. O., Jen, T.-C., Ren, J. & van Duin, A. Towards the realisation of high perm-selective MoS₂ membrane for water desalination. *Npj Clean. Water* **6**, 1–15 (2023).
- Kim, S. et al. Neuromorphic van der Waals crystals for substantial energy generation. *Nat. Commun.* **12**, 47 (2021).

8. Kwon, K. C., Baek, J. H., Hong, K., Kim, S. Y. & Jang, H. W. Memristive devices based on two-dimensional transition metal chalcogenides for neuromorphic computing. *Nano-Micro Lett.* **14**, 58 (2022).
9. Hille, B. Ionic channels in excitable membranes. *Curr. Probl. Biophys. Approaches Biophys. J.* **22**, 283–294 (1978).
10. Mei, T. et al. Ionic Transistors. *ACS Nano* **18**, 4624–4650 (2024).
11. Karnik, R. et al. Electrostatic control of ions and molecules in nanofluidic transistors. *Nano Lett.* **5**, 943–948 (2005).
12. Cheng, C., Jiang, G., Simon, G. P., Liu, J. Z. & Li, D. Low-voltage electrostatic modulation of ion diffusion through layered graphene-based nanoporous membranes. *Nat. Nanotechnol.* **13**, 685–690 (2018).
13. Wang, Y. et al. Voltage-gated ion transport in two-dimensional sub-1 nm nanofluidic channels. *ACS Nano* **13**, 11793–11799 (2019).
14. Xue, Y. et al. Atomic-scale ion transistor with ultrahigh diffusivity. *Science* **372**, 501–503 (2021).
15. Saini, L., Nemala, S. S., Rath, A., Kaushik, S. & Kalon, G. Selective transport of water molecules through interlayer spaces in graphite. *Nat. Commun.* **13**, 498 (2022).
16. Kalman, E. B., Sudre, O., Vlassioun, I. & Siwy, Z. S. Control of ionic transport through gated single conical nanopores. *Anal. Bioanal. Chem.* **394**, 413–419 (2009).
17. Cantley, L. et al. Voltage gated inter-cation selective ion channels from graphene nanopores. *Nanoscale* **11**, 9856–9861 (2019).
18. Su, S. et al. Multifunctional graphene heterogeneous nano-channel with voltage-tunable ion selectivity. *Nat. Commun.* **13**, 4894 (2022).
19. Cheng, M. et al. Rational fabrication of MXene/graphene oxide membrane and its voltage-gated ion transport behavior. *ACS Sustain. Chem. Eng.* **9**, 7206–7210 (2021).
20. Ouyang, H. et al. Facile preparation of a MXene–graphene oxide membrane and its voltage-gated ion transport behavior. *Phys. Chem. Chem. Phys.* **24**, 27157–27162 (2022).
21. Li, D., Jing, W., Li, S., Shen, H. & Xing, W. Electric field-controlled ion transport in TiO₂ nanochannel. *ACS Appl. Mater. Interfaces* **7**, 11294–11300 (2015).
22. Qiu, Y., Ma, J. & Chen, Y. Ionic behavior in highly concentrated aqueous solutions nanoconfined between discretely charged silicon surfaces. *Langmuir* **32**, 4806–4814 (2016).
23. Kalluri, R. K., Konatham, D. & Striolo, A. Aqueous NaCl solutions within charged carbon-slit pores: partition coefficients and density distributions from molecular dynamics simulations. *J. Phys. Chem. C* **115**, 13786–13795 (2011).
24. Köpfer, D. A. et al. Ion permeation in K⁺ channels occurs by direct Coulomb knock-on. *Science* **346**, 352–355 (2014).
25. Rath, A. et al. Anomalous transport in angstrom-sized membranes with exceptional water flow rates and dye/salt rejections. *Mater. Today Nano* **22**, 100328 (2023).
26. Aparna, R., Biswabhusan, D., Sarath, S. S. & Gopinadhan, K. Ion-hydration-controlled large osmotic power with arrays of angstrom scale capillaries of vermiculite. *Cell Rep. Phys. Sci.* **4**, 101717 (2023).
27. Walker, G. F. & Garrett, W. G. Chemical exfoliation of vermiculite and the production of colloidal dispersions. *Science* **156**, 385–387 (1967).
28. Xia, Z. et al. Tunable ion transport with freestanding vermiculite membranes. *ACS Nano* **16**, 18266–18273 (2022).
29. Wang, J. et al. Unlocking osmotic energy harvesting potential in challenging real-world hypersaline environments through vermiculite-based hetero-nanochannels. *Nat. Commun.* **15**, 608 (2024).
30. Hu, J., Xiao, X.-D., Ogletree, D. F. & Salmeron, M. Imaging the condensation and evaporation of molecularly thin films of water with nanometer resolution. *Science* **268**, 267–269 (1995).
31. Grahame, D. C. The electrical double layer and the theory of electrocapillarity. *Chem. Rev.* **41**, 441–501 (1947).
32. Surti, P., Kailasa, S. K., Mungray, A., Park, T. J. & Mungray, A. K. Vermiculite nanosheet augmented novel proton exchange membrane for microbial fuel cell. *Fuel* **357**, 130046 (2024).
33. Chen, Y. et al. Cation-intercalated clay-based two-dimensional membranes for effective desalination and molecule sieving. *ACS Appl. Mater. Interfaces* **16**, 1749–1756 (2024).
34. Todea, M., Vanea, E., Bran, S., Berce, P. & Simon, S. XPS analysis of aluminosilicate microspheres bioactivity tested in vitro. *Appl. Surf. Sci.* **270**, 777–783 (2013).
35. Kądziołka-Gaweł, M., Czaja, M., Dulski, M., Krzykowski, T. & Szubka, M. Impact of high temperatures on aluminoceladonite studied by Mössbauer, Raman, X-ray diffraction and X-ray photoelectron spectroscopy. *Mineral. Petrol.* **115**, 431–444 (2021).
36. Raidongia, K. & Huang, J. Nanofluidic ion transport through reconstructed layered materials. *J. Am. Chem. Soc.* **134**, 16528–16531 (2012).
37. Tansel, B. Significance of thermodynamic and physical characteristics on permeation of ions during membrane separation: Hydrated radius, hydration free energy and viscous effects. *Sep. Purif. Technol.* **86**, 119–126 (2012).
38. Roux, B. The membrane potential and its representation by a constant electric field in computer simulations. *Biophys. J.* **95**, 4205–4216 (2008).
39. Doyle, D. A. et al. The structure of the potassium channel: molecular basis of K⁺ conduction and selectivity. *Science* **280**, 69–77 (1998).
40. Violet, C. et al. Designing membranes with specific binding sites for selective ion separations. *Nat. Water* **2**, 706–718 (2024).
41. Singh, K. P. & Kumar, M. Effect of gate length and dielectric thickness on ion and fluid transport in a fluidic nanochannel. *Lab. Chip* **12**, 1332 (2012).
42. Maruvada, A., Shubhakar, K., Raghavan, N., Pey, K. L. & O'Shea, S. J. Dielectric breakdown of 2D muscovite mica. *Sci. Rep.* **12**, 14076 (2022).
43. Liu, Y. et al. Pillared laminar vermiculite membranes with tunable monovalent and multivalent ion selectivity. *Adv. Mater.* **37**, 2417994 (2025).
44. Pouvreau, M., Greathouse, J. A., Cygan, R. T. & Kalinichev, A. G. Structure of hydrated gibbsite and brucite edge surfaces: DFT results and further development of the ClayFF classical force field with metal–O–H Angle Bending Terms. *J. Phys. Chem. C* **121**, 14757–14771 (2017).
45. Berendsen, H. J. C., Postma, J. P. M., van Gunsteren, W. F. & Hermans, J. Interaction models for water in relation to protein hydration. *Intermolecular Forces: Proc. Fourteenth Jerus. Symp. Quantum Chem. Biochem. Held Jerus.* **14**, 331–342 (1981).
46. Páll, S. et al. Heterogeneous parallelization and acceleration of molecular dynamics simulations in GROMACS. *J. Chem. Phys.* **153**, 134110 (2020).
47. Abraham, M. J. et al. GROMACS: High performance molecular simulations through multi-level parallelism from laptops to supercomputers. *SoftwareX* **1–2**, 19–25 (2015).
48. Stukowski, A. Visualization and analysis of atomistic simulation data with OVITO—the Open Visualization Tool. *Model. Simul. Mater. Sci. Eng.* **18**, 015012 (2009).

Acknowledgements

This work was mainly funded by DST-INAIE with grant no. 2023/IN-TW/09. We also acknowledge the financial support from MHRD STARS with grant no. MoE-STARS/STARS-1/405 and by Science and Engineering Research Board (SERB), Government of India, through grant no. CRG/2023/004818. K.G. acknowledges the support of Kanchan and Harilal Doshi chair fund. C.N. acknowledges the support from IASc-INSA-NASI in the form of Focus Area Science Technology Summer Fellowship. The authors acknowledge the contribution from IITGN central instrumentation facility, especially the FIST-DST system with grant no. SR/FST/PS-1/

2020/141. L.H.Y. acknowledges the financial support from the National Science and Technology Council (NSTC), Taiwan under Grant No. NSTC 112-2923-E-011-003-MY3. Use of computational resources was supported by NSF under the ACCESS program, award no. PHY250014, to Y.N.

Author contributions

K.G. conceived the idea and supervised the project. D.B. designed the project, executed the sample preparation, characterization, voltage gating measurements, and result analysis. Y.N. carried out the MD simulation and result analysis. S.N.P. helped in the result analysis. C.N. helped in the sample preparation and initial optimization of the voltage-gating measurements. S.S.N. carried out the Raman and XPS measurements. R.A. helped in optimizing the membrane stability and zeta potential measurements. K.S. helped in the XRD measurement. A.C. and L.H.Y. helped in the data analysis. S.K.N. helped in the theoretical analysis. D.B., Y.N. and K.G. wrote the manuscript. All the authors discussed the results and commented on the manuscript.

Competing interests

The authors declare no competing interests.

Additional information

Supplementary information The online version contains supplementary material available at <https://doi.org/10.1038/s41467-025-62737-3>.

Correspondence and requests for materials should be addressed to Kalon Gopinadhan.

Peer review information *Nature Communications* thanks Sridhar Komarneni, Yunliang Zhao, and the other, anonymous, reviewer(s) for their contribution to the peer review of this work. A peer review file is available.

Reprints and permissions information is available at <http://www.nature.com/reprints>

Publisher's note Springer Nature remains neutral with regard to jurisdictional claims in published maps and institutional affiliations.

Open Access This article is licensed under a Creative Commons Attribution-NonCommercial-NoDerivatives 4.0 International License, which permits any non-commercial use, sharing, distribution and reproduction in any medium or format, as long as you give appropriate credit to the original author(s) and the source, provide a link to the Creative Commons licence, and indicate if you modified the licensed material. You do not have permission under this licence to share adapted material derived from this article or parts of it. The images or other third party material in this article are included in the article's Creative Commons licence, unless indicated otherwise in a credit line to the material. If material is not included in the article's Creative Commons licence and your intended use is not permitted by statutory regulation or exceeds the permitted use, you will need to obtain permission directly from the copyright holder. To view a copy of this licence, visit <http://creativecommons.org/licenses/by-nc-nd/4.0/>.

© The Author(s) 2025